A Moiré Microscope for Finite Deformation Micro-mechanical Studies

by N.-S. Liou and V. Prakash

ABSTRACT—A new version of a moiré microscope is presented that embodies the theory of optical moiré interferometry. To interrogate the deformed specimen grating, the device uses a transmission diffraction grating that allows for a simple and quick change of the virtual reference grating vector without disturbing the optical alignment of the other components in the optical train. To analyze deformation from the acquired moiré interference fringe patterns, the displacement light-intensity moiré optical law introduced by Sciammarella is revisited. The analysis of deformation is consistent with the continuum principles of finite deformation and can readily be used to obtain micro-mechanical quantities of interest such as the local strains, stretches and rotations.

KEY WORDS—Computer vision/digital image processing, electronic recording interferometry, interferometric moiré, plasticity

Introduction

Moiré interferometry, or more precisely moiré interference fringes, has existed in the field of optics since 1874.[2] Approximately 50 years ago, its application as a measuring tool for displacement analysis was developed.[3] The most common form of this technique has been the geometric interference moiré,[4–7] which is still the easiest form of this technique to implement. For a long period of time, the application of moiré fringes to the analysis of displacement was hindered by the precision that could be achieved in the measurement of displacements. Because the smallest displacement that could be detected is dependent on the pitch of the grid used, in order to increase the sensitivity of the moiré method it is highly desirable to increase the frequency of the grid lines. With the advent of lasers and very precise methods to produce submicron scale diffraction gratings, the theory of geometric interference moiré has been extended to optical interference moiré, which involves length scales and resolutions achieved with optical interference.

The moiré microscope, which is an implementation of optical interference moiré, is a relatively new apparatus and is currently being used as a research tool to study localized deformation conditions and/or microscopic events. The method uses an optical microscope to achieve the desired spatial resolution for micro-mechanics studies. Shield and Kim[8] introduced an optical interference moiré microscope with an ability to vary the virtual reference grating in order to maintain a fringe spacing for maximum accuracy. Han and Post[9] extended the sensitivity of moiré interferometry by an order of magnitude using an immersion interferometer and optical/digital fringe multiplication. Recently, Zou *et al.*[10] developed a multipurpose macro/micro moiré interferometer capable of both macro and micro measurements simultaneously. The experimental technique of electron beam moiré was introduced by Dally and Read[11] for determining micro-mechanical deformation.

For finite deformation studies, there is a practical limitation to the frequency of grid lines that can be used. Sciammarella and Durelli[12] and Sciammarella,[1] in an attempt to increase the sensitivity of the technique without increasing the frequency of the moiré grid lines, introduced a displacement light-intensity moiré optical law for the analysis of discrete geometric and optical moiré fringes. Theoretically, the algorithm has a tremendous potential for increasing the resolution by which the displacements can be calculated from the moiré interference fringe pattern. In recent years, as digital image processing has become easily accessible, numerous image-processing methods have been developed to complement interferometric measurement techniques. For example, a series of fringe or phase-shifted interferograms are used to compute fringe order at every pixel in the field[13] or to provide a contour map with discrete fractional fringe orders.[14]

Motivated by these developments and realizing the need to extend moiré to finite elastic-plastic deformation, a new version of the optical moiré microscope developed is presented. This optical device allows for simple and quick sensitivity adjustment without disturbing the optical alignment of other components in the optical train. This is achieved by employing a transmission diffraction grating to create a variable virtual reference grating vector for the interrogation of the deformed surface grating. Besides being useful in generating u and v displacement field interference fringe patterns, the change in magnitude, as well as the direction of the virtual reference grating vector, facilitates the generation of moiré fringes with gradual changes in slope even for cases in which sharp transitions/localization in surface deformation are present. Also, an interactive image-processing program based on a digital implementation of the displacement light-intensity law introduced by Sciammarella[1] is developed within the MATLAB programming environment. The deformation analysis is consistent with the continuum principles of finite deformation and can readily be used to obtain local micro-mechanical quantities of interest such as the deformation gradient tensor, the Almansi strain tensor, principal stretches (and their directions) and the finite rotation tensor.

N.-S. Liou is a Graduate Student, and V. Prakash is an Associate Professor, Department of Mechanical and Aerospace Engineering, Case Western Reserve University, Cleveland, OH 44106-7222.

Original manuscript submitted: September 21, 1998.
Final manuscript received: March 25, 2000.

Theoretical Formulation

To relate moiré interference fringes to deformation analysis, we appeal to the basic principles of classical continuum mechanics. Figure 1 shows, schematically, the continuum mechanics representation of the deformation process, in which a vector **dX**, represented by the letters A and B in the undeformed configuration, is mapped during the deformation to a new vector **dx**, represented by the points A' and B' in the deformed configuration. The specimen grating in the undeformed configuration can be represented by the *reciprocal specimen grating vector*, **G**. The direction of the vector **G** is perpendicular to the specimen grating lines, while its magnitude is determined by the reciprocal of the pitch of the specimen grating in the undeformed configuration. Thus, for a constant linear specimen grating, the magnitude of the vector **G** is given by

$$|\mathbf{G}| = \frac{1}{D}, \tag{1}$$

where D is the pitch of the undeformed specimen grating. In view of eq (1), the number of grid lines of the specimen grating intercepted by the vector **dX** in the undeformed configuration is given by $\mathbf{G} \cdot \mathbf{dX}$.

Like the reciprocal specimen grating vector, the *reciprocal reference grating vector*, **g**, is defined to be perpendicular to the reference virtual grating lines, and its magnitude is equal to the reciprocal of the pitch of the reference grating lines, d, that is,

$$|\mathbf{g}| = \frac{1}{d}. \tag{2}$$

Thus, the number of reference grating lines intercepted by the vector **dx** in the deformed configuration is given by $\mathbf{g} \cdot \mathbf{dX}$.

In accordance with the principles of the geometric moiré, the number of moiré fringes intercepted by the vector **dx** in the deformed configuration is given by the difference in the number of the virtual reference grating lines and the specimen grating lines in between the points A' and B'. For one-to-one deformation mapping, the number of specimen grid lines in between the points A' and B' is the same as the number of grating lines in between the points A and B in the undeformed configuration, that is, $\mathbf{G} \cdot \mathbf{dX}$. Thus, the number of fringe lines df intercepted by the vector **dx** is given by

$$df = \mathbf{g} \cdot \mathbf{dx} - \mathbf{G} \cdot \mathbf{dX}. \tag{3}$$

In eq (3), the reciprocal grating vectors **g** and **G** are known a priori. By selecting a vector **dx** in the deformed configuration and counting the number of fringes intercepted by the vector **dx**, the unknown vector **dX** can be determined. Once the vectors **dx** and **dX** are known, the deformation gradient tensor **F** can readily be calculated.

Unlike the geometrical interference moiré, the theory of optical interference moiré relies on the theory of light diffraction. More specifically, the technique relies on measuring the change in the phase of light beams diffracted from a specimen grating. Figure 2 illustrates the basic principle behind the optical interference moiré. Two collimated but nonparallel beams of laser light are passed through a lens that redirects them along directions denoted by propagation vectors $\mathbf{k}^{(1)}$ and $\mathbf{k}^{(2)}$ to form an illumination volume at the specimen surface. Upon interaction with the deformed specimen grating, each of these input beams results in a set of diffracted beams. Only the Mth diffraction order corresponding to the $\mathbf{k}^{(1)}$ input beam and the Nth diffraction order corresponding to the $\mathbf{k}^{(2)}$ input beam are shown. Many other diffraction orders are present and can be used to produce moiré interference fringes at the image plane. Typically, ± 1 diffraction orders are used for interference.

The irradiance $I(\mathbf{x})$ corresponding to the interference of the selected diffraction orders is obtained by taking the dot product of the resultant electric field, $\mathbf{E_R}$, and its complex conjugate, $\bar{\mathbf{E}}_\mathbf{R}$. For the present case, $\mathbf{E_R}$ can be written as

$$\mathbf{E_R} = \mathbf{E_M^{(1)}} + \mathbf{E_N^{(2)}}, \tag{4}$$

where $\mathbf{E_M^{(1)}}$ represents the electric field vector for the Mth diffracted beam corresponding to the $\mathbf{k}^{(1)}$ input beam and $\mathbf{E_N^{(2)}}$ is the electric field vector for the Nth diffracted beam

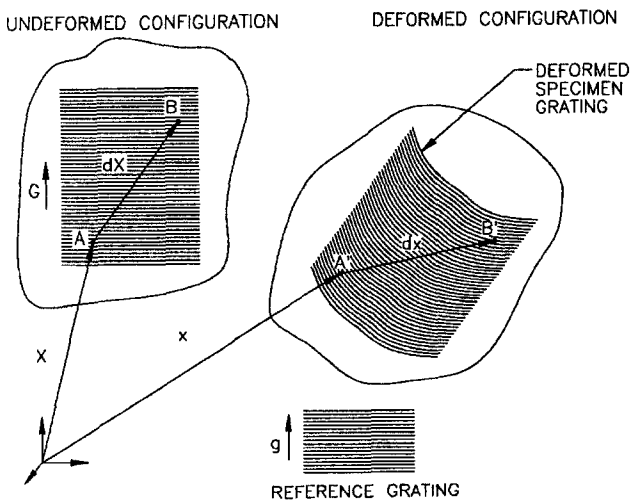

Fig. 1—Schematic of the continuum mechanics representation of the deformation process showing the reference and the deformed configurations

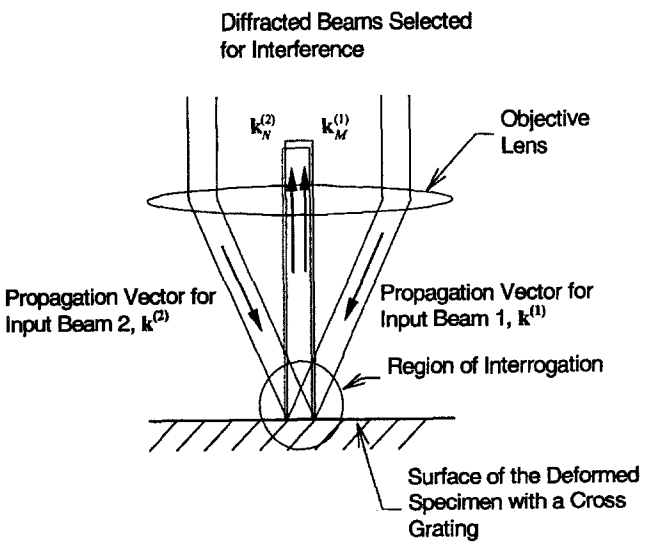

Fig. 2—Schematic illustrating the basic principle of optical interference moiré

corresponding to the $\mathbf{k}^{(2)}$ input beam. The resultant irradiance, or power, at the specimen is given by

$$I(\mathbf{x}) = \mathbf{E_R} \cdot \bar{\mathbf{E}}_\mathbf{R}. \tag{5}$$

Following Shield and Kim,[8] the expression for irradiance $I(\mathbf{x})$ can be written as

$$I(\mathbf{x}) = I_M^{(1)}(\mathbf{x}) + I_N^{(2)}(\mathbf{x}) + 2\sqrt{I_M^{(1)}(\mathbf{x}) I_N^{(2)}(\mathbf{x})}\cos\psi(\mathbf{x}), \tag{6}$$

where $I_M^{(1)} = \left|\mathbf{A}_\mathbf{M}^{(1)}\right|^2$, $I_N^{(2)} = \left|\mathbf{A}_\mathbf{N}^{(2)}\right|^2$ and

$$\psi(\mathbf{x}) = \left(\mathbf{k}^{(1)} - \mathbf{k}^{(2)}\right) \cdot \mathbf{x} + 2\pi(M - N)\mathbf{G} \cdot (\mathbf{X} - \mathbf{X_0}) + \phi_o. \tag{7}$$

In eq (7), $\mathbf{X}$ is the material point corresponding to the point $\mathbf{x}$ in the deformed configuration, $\mathbf{X}_o$ is a reference point on the specimen grid and ϕ_o represents the relative phase difference between the two input beams $\mathbf{k}^{(1)}$ and $\mathbf{k}^{(2)}$.

In view of eq (7), the fringe number f, at a location x in the deformed configuration, can be written as

$$f - f_o = \frac{\left(\mathbf{k}^{(1)} - \mathbf{k}^{(2)}\right)}{2\pi} \cdot \mathbf{x} + (M - N)\mathbf{G} \cdot (\mathbf{X} - \mathbf{X_0}), \tag{8}$$

where $f_o = \phi_o/2\pi$. Equation (8) has the same form as the equation for geometric moiré, and it becomes identical to eq (3) if the *effective reciprocal grating vector*, $\hat{\mathbf{g}}$, and the *effective specimen grating vector*, $\hat{\mathbf{G}}$, are defined such that

$$\hat{\mathbf{g}} = \frac{\mathbf{k}^{(1)} - \mathbf{k}^{(2)}}{2\pi} \quad \text{and} \quad \hat{\mathbf{G}} = (N - M)\mathbf{G}, \tag{9}$$

respectively.

Deformation Analysis Using Moiré Interference Images

The ultimate goal of the moiré microscope is to interrogate the specimen in situ or after deformation to obtain a full-field measurement of the deformation field. Because it is desirable to use the moiré microscope apparatus to study finite elastic-plastic deformations, a formulation consistent with large deformation is required. Also, since the moiré fringes are recorded on the deformed configuration, a Eulerian material description is the preferred choice.

To carry out the finite deformation analysis, we must calculate the deformation gradient tensor $\mathbf{F}$ from the moiré interference fringe patterns. To obtain the components $\mathbf{F}$, two effective virtual reference grating vectors, $\hat{\mathbf{g}}^{(1)}$ and $\hat{\mathbf{g}}^{(2)}$, and two effective specimen grating vectors, $\hat{\mathbf{G}}^{(1)}$ and $\hat{\mathbf{G}}^{(2)}$, are required. The use of two specimen grating and two virtual reference grating vectors can be interpreted in physical terms as the illumination of a crossed specimen grating with two different orientations of the virtual reference grating. From here onward, for the sake of convenience, the hats will be dropped while writing the vectors $\hat{\mathbf{g}}$ and $\hat{\mathbf{G}}$.

Taking the gradient of eq (8) with respect to the coordinate $\mathbf{x}$ in the deformed configuration yields

$$\frac{\partial f^{(1)}}{\partial x_j} = g_j^{(1)} - F_{ji}^{-T} G_i^{(1)} \tag{10}$$

$$\frac{\partial f^{(2)}}{\partial x_j} = g_j^{(2)} - F_{ji}^{-T} G_i^{(2)}. \tag{11}$$

Next, defining a second-order specimen grating tensor $\mathbf{\Gamma}$ as

$$\Gamma_{ik} = G_i^{(1)} G_k^{(1)} + G_i^{(2)} G_k^{(2)}, \tag{12}$$

and a second-order tensor $\mathbf{H}$ by

$$H_{jk} = \left(g_j^{(1)} - \frac{\partial f^{(1)}}{\partial x_j}\right) G_k^{(1)} + \left(g_j^{(2)} - \frac{\partial f^{(2)}}{\partial x_j}\right) G_k^{(2)}, \tag{13}$$

the deformation gradient tensor $\mathbf{F}$ can be expressed as

$$\mathbf{F} = \mathbf{H}^{-T}\mathbf{\Gamma}^T. \tag{14}$$

Equation (14) relates the deformation gradient tensor to the effective specimen grating vector $\mathbf{G}$, the virtual effective reference grating $\mathbf{g}$ and the measured fringe gradients with respect to the deformed configuration.

Once the local deformation gradient tensor is obtained, the local left Cauchy Green tensor, $\mathbf{B}$, can be calculated using

$$\mathbf{B} = \mathbf{F}\mathbf{F}^T. \tag{15}$$

Because the tensor $\mathbf{B}$ is symmetric and positive definite, a unique positive definite and symmetric tensor $\mathbf{V}$ (also known as the left stretch tensor) exists such that

$$\mathbf{V}^2 = \mathbf{B}. \tag{16}$$

In view of the spectral theorem,[15] the spectral decomposition of $\mathbf{B}$ yields

$$\mathbf{B} = \lambda_1^2\, \boldsymbol{\xi}_1 \otimes \boldsymbol{\xi}_1 + \lambda_2^2\, \boldsymbol{\xi}_2 \otimes \boldsymbol{\xi}_2, \tag{17}$$

where λ_i are the eigenvalues of the tensor $\mathbf{B}$ and represent the two principal stretches and $\boldsymbol{\xi}_1$ and $\boldsymbol{\xi}_2$ are the corresponding eigenvectors representing the principal stretch directions. Then, in view of the square root theorem,[15] the spectral decomposition of the right stretch tensor $\mathbf{V}$ can be written as

$$\mathbf{V} = \lambda_1\, \boldsymbol{\xi}_1 \otimes \boldsymbol{\xi}_1 + \lambda_1\, \boldsymbol{\xi}_2 \otimes \boldsymbol{\xi}_2. \tag{18}$$

Once the local deformation gradient tensor $\mathbf{F}$ and the local left stretch tensor $\mathbf{V}$ are known, the local rotation tensor $\mathbf{R}$ can be conveniently calculated by employing the left polar decomposition theorem,[15] that is,

$$\mathbf{R} = \mathbf{V}^{-1}\mathbf{F}. \tag{19}$$

Also, once the local deformation gradient tensor is known, the finite deformation Almansi strain tensor $\mathbf{E}^\mathbf{A}$ can be calculated using

$$\mathbf{E}^\mathbf{A} = \frac{1}{2}\left[\mathbf{I} - (\mathbf{F} \cdot \mathbf{F}^T)^{-1}\right]. \tag{20}$$

Description of the Moiré Microscope

The configuration of the moiré microscope is shown schematically in Fig. 3. A 5 mW He-Ne laser (a) is used for system illumination. The beam is filtered, expanded and collimated to produce a source with no wave front disturbances. Next, a primary lens (b) is used for two purposes: (1) to ensure a collimated beam at the specimen for illumination and (2) to make the task of masking the unwanted diffraction orders much easier by focusing the beams diffracted by the transmission grating. The primary lens is placed such that its distance from the objective lens is equal to the sum of the focal lengths of both lenses. This ensures that the beams upon going through the focal point of the primary lens remain collimated after entering the objective lens. The next component in the optical train is the transmission diffraction grating subassembly (c). The transmission diffraction grating employed has a frequency of 12 lines/mm and is used for creating the two input illumination beams, $\mathbf{k}^{(1)}$ and $\mathbf{k}^{(2)}$. The use of the transmission grating subassembly makes it possible to adjust the sensitivity of the moiré apparatus continuously and without disturbing the optical alignment of the other critical elements in the optical train. This is accomplished by simply translating the transmission grating forward or backward along the system optical axis, which changes the angle that the input beams make with the optical axis and, hence, changes the magnitude of the effective virtual reference grating vector, $\mathbf{g}$. In addition, the transmission grating subassembly is allowed to rotate about the optical axis of the objective lens, which results in a change in the direction of the vector $\mathbf{g}$. Thus, besides generating the $\mathbf{u}$ and $\mathbf{v}$ field fringe patterns, the change in magnitude of the virtual grating vector facilitates maintaining an optimum fringe spacing for maximum accuracy, whereas the change in direction of the virtual grating vector facilitates the generation of moiré fringes with gradual change in slope even for cases in which there are sharp transitions (localizations) in surface deformation. Next, the input beam mask (d) is used to allow only the necessary diffracted beams to pass. This mask consists of a thin piece of metal painted black to absorb any light that might otherwise diffract or scatter. In the present configuration, the mask is used to block the zeroth order and all the higher order diffraction beams, except the ± 1-order diffracted beams. Next, the input beams (i.e., the ± 1-order diffracted beams) enter the objective lens at (f) and are redirected to form the illumination volume near the specimen (g) surface. The illumination beams, after diffraction by the deformed specimen grating, travel back toward the objective lens (f) and are redirected toward the iris at (h) by the use of the cube beam splitter at (e). The iris is then used to select the desired diffraction orders for forming the moiré interference images and acts as a filter for the other diffraction orders. Thus, the illumination from only the desired diffraction orders reaches the image plane at (i). A Sony SSC-C374 CCD camera, placed at the image plane, is used to collect the moiré interference fringe patterns for input into the image acquisition system. The magnification of the image can be changed by simply moving the camera closer to or farther away from the iris. The output of the digital camera is connected to an image acquisition system that allows images to be stored and manipulated on the computer. The image acquisition system (j) consists of a 200 MHz Pentium processor PC with a frame-grabber card. The frame-grabber card stores each frame as a 512×480 array of 256 gray levels. An additional monitor is used for real-time viewing of the image, selection of regions of interest and scaling. To increase the sensitivity and fringe contrast, a phase shift wedge is placed in any one of the two legs of the illumination beams (described in detail in the results section). Once the image is digitized and saved as a file, it is loaded into an image-processing software based on MATLAB for deformation analysis.

Calibration of the Moiré Microscope

A crossed diffraction grating with a frequency of 185 lines/mm was used for calibrating the moiré microscope. During the calibration process, the distance between the transmission diffraction grating and the objective lens, as well as the angular orientation of the transmission grating with respect to the optical axis, is related to the magnitude and the direction of the effective virtual reference grating vector, $\mathbf{g}$.

The first step in the calibration process is to align the specimen and the virtual reference grating such that a null field is obtained. Next, by systematically translating and rotating the transmission diffraction grating, that is, by changing the input vectors $\mathbf{k}^{(1)}$ and $\mathbf{k}^{(2)}$, various virtual reference grating vectors are generated. Corresponding to each virtual reference grating vector, a fringe pattern depicting carrier fringes is obtained. These carrier fringes are the result of a mismatch between the virtual reference grating vector and the undeformed specimen grating vector. For calibration purposes, the spacing and the direction of the carrier fringes are related to the linear position and the angular orientation of the transmission diffraction grating.

The creation and the mapping of the input beams are shown schematically in Fig. 4(a). The variable d represents the distance of the transmission diffraction grating from the objective lens. The remaining calibration variables are defined as follows: β_J is the angle of the Jth-order diffracted beam from the transmission diffraction grating, a is the distance between the input beam and the optical axis at the objective lens, l_f is the focal length of the objective lens and Δ is the excess distance from the focal length of the objective lens at which the input beams intersect the optical axis due to the nonparallelity of the input beams with the optical axis. Figure 4(b) shows schematically the two input beams along the vectors $\mathbf{k}^{(1)}$ and $\mathbf{k}^{(2)}$, which interfere to form the virtual reference grating vector. In view of eq (9), the magnitude of the virtual reciprocal grating vector can be expressed as

$$|\mathbf{g}| = \frac{2 \sin \alpha}{\lambda}. \tag{21}$$

From Fig. 4(b), the input angle α can be expressed as

$$\alpha = \tan^{-1}\left(\frac{a-h}{l_f}\right), \tag{22}$$

where

$$a = d \tan \beta_J \quad \text{and} \quad h = 1_f \tan \beta_J. \tag{23}$$

Thus, in view of eqs (21) through (23), the magnitude of the reference grating reciprocal vector can be represented in terms of the known quantities, that is, the distance between the transmission grating and the objective lens d, the focal length of the objective lens l_f and the diffraction angle β_J.

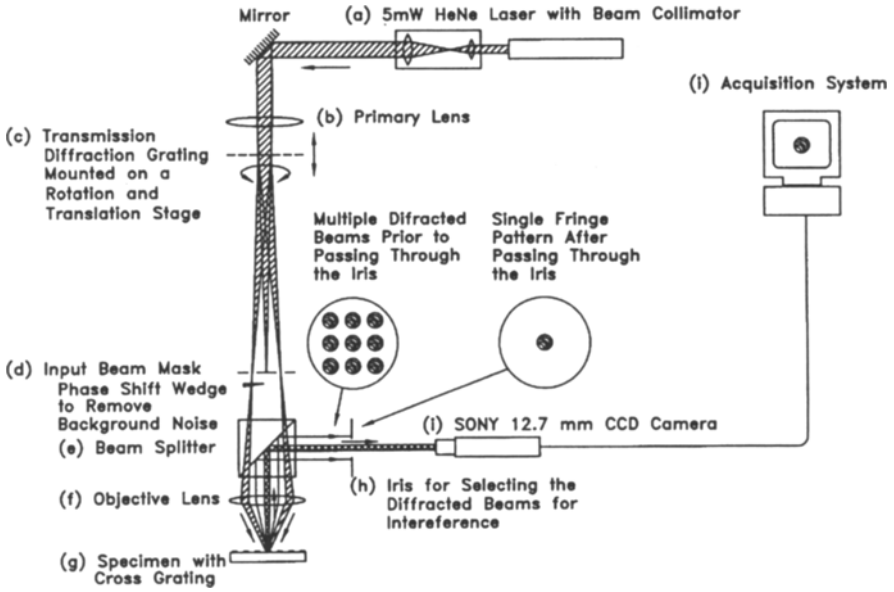

Fig. 3—Schematic of the moiré microscope

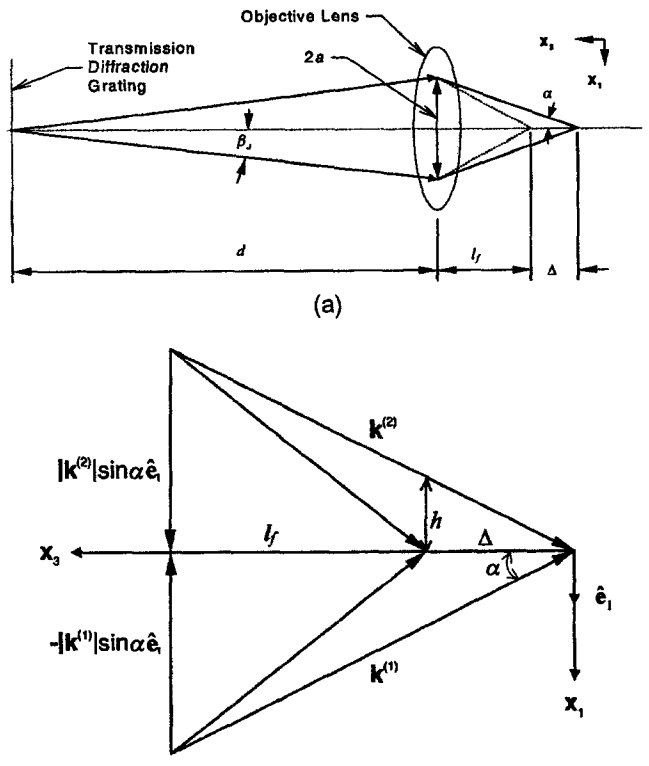

Fig. 4—(a) Geometric representation showing the mapping of the input beams on the specimen surface, (b) vectorial representation showing the interference of the two input beams to form the reference grating vector

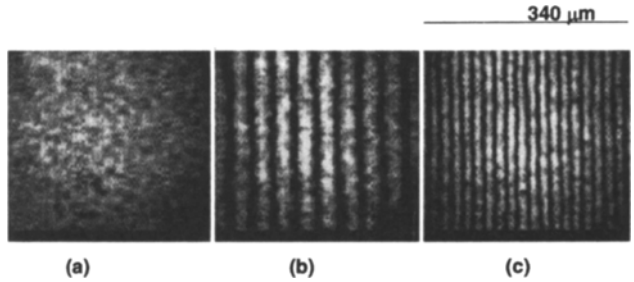

Fig. 5— Moiré interference fringe pattern showing carrier fringes corresponding to $J = \pm 1$ and a transmission grating with a frequency of 12 lines/mm: (a) $d = 300$ mm and $\theta = 0$ deg (null field), (b) $d = 320$ mm and $\theta = 0$ deg, (c) $d = 340$ mm $\theta = 0$ deg

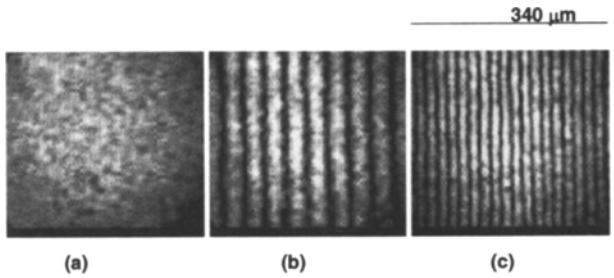

Fig. 6—Moiré interference fringe pattern showing carrier fringes corresponding to $J = \pm 1$ and a transmission grating with a frequency of 12 lines/mm: (a) $d = 300$ mm and $\theta = 90$ deg (null field), (b) $d = 320$ mm and $\theta = 90$ deg, (c) $d = 340$ mm $\theta = 90$ deg

Figures 5(a) to 5(c) show the carrier fringes corresponding to $d = 300$ mm, $d = 320$ mm and $d = 340$ mm, respectively, for $J = \pm 1$, $\theta = 0$ deg and a transmission grating with a frequency of 12 lines/mm. The distance $d = 300$ mm corresponds to the null-field condition, that is, $\mathbf{g}^{(1)} = \mathbf{G}^{(1)}$. Figures 6(a) to 6(c) show the carrier fringe patterns corresponding to $d = 300$ mm, $d = 320$ mm and $d = 340$ mm, respectively, obtained by rotating the virtual reference grating vector $\mathbf{g}^{(1)}$ by 90 deg. Again, $d = 300$ mm corresponds to the null-field case.

Experimental Results: Digital Data Processing and Deformation Analysis

The specimen used to demonstrate the digital image-processing and deformation analysis capabilities of the moiré

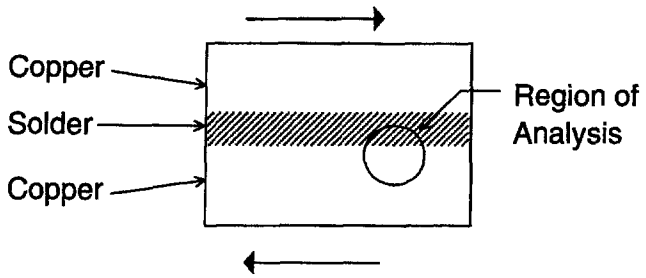

Fig. 7—Schematic of the copper-solder-copper sandwich specimen employed in the experiments

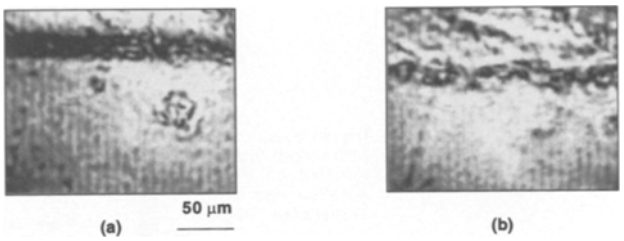

Fig. 8—(a) **u**-field and (b) **v**-field moiré interference fringe patterns obtained after loading the copper-solder-copper sandwich specimen in shear

microscope comprises a thin layer of solder sandwiched between two copper plates, and is shown schematically in Fig. 7. The solder layer is loaded primarily in shear by displacing the top copper plate approximately parallel to the lower copper plate. Because the flow stress of solder is much lower than that of the copper plates, the solder deforms plastically in between the copper plates. Prior to the deformation, a crossed grating is applied to a lapped and polished face of the specimen using the replication technique.[3] In this process, silicon rubber submaster grating is replicated from master gratings with a frequency of 185 lines/mm. A pool of liquid adhesive (PC-10, Measurements Group) is poured on this submaster grating mold. The submaster mold is then pressed against the specimen. Because silicon rubber is a nonstick material, the mold and specimen can be separated easily after the adhesive solidifies, leaving behind a crossed diffraction grating on the specimen surface.

Figures 8(a) and 8(b) show the **u** and **v** field moiré interference fringe patterns, respectively, obtained after loading the composite specimen. From these images, it is difficult to carry out the deformation analysis with sufficient accuracy, since these interference images have too few moiré fringes. To overcome this difficulty, the virtual reference grating vector, **g**, is varied to add carrier fringes to the interference images. As discussed in the previous section, the virtual reference grating vector can be varied (1) by translating the transmission along the optical axis of the apparatus, (2) by rotating the transmission grating about the optical axis and (3) by providing a combined translation and rotation to the transmission grating.

Figures 9(a) and 9(b) show the **u**-field moiré interference images for six different virtual reference grating vectors obtained by translation and rotation of the transmission diffraction grating along the optical axis. The distance $d = 300$ mm and $\theta = 0$ deg [see Fig. 9(a)] corresponds to the initial null-field configuration, that is, $\mathbf{g} = \mathbf{G}$. Figure 9(b) corresponds to $d = 306.5$ mm and $\theta = 0$ deg, while Fig. 9(c) corresponds to $d = 313$ mm and $\theta = 0$ deg. By changing the magnitude of the **g** vector (i.e., by only translating the transmission diffraction grating), a significant number of carrier fringes were added to the null-field moiré interference image. Figures 9(d) and 9(e) show the moiré interference images obtained by only rotating (no translation) the transmission diffraction grating. Figure 9(d) corresponds to $d = 300$ mm and $\theta = 1$ deg, whereas Fig. 9(e) corresponds to $d = 300$ mm and $\theta = -1$ deg. Figure 9(f) is obtained by providing a combined translation and rotation to the transmission diffraction

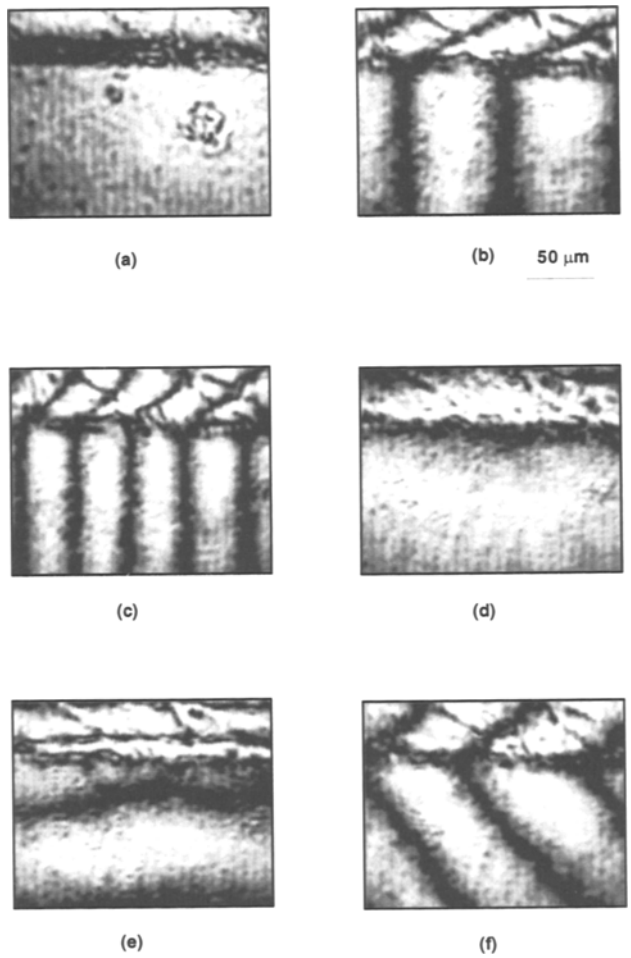

Fig. 9—**u**-field moiré interference fringe patterns for six different virtual reference grating vectors obtained by translation and rotation of the transmission diffraction grating along the optical axis corresponding to $J = \pm 1$ and (a) $d = 300$ mm and $\theta = 0$ deg (null field), (b) $d = 306.5$ mm and $\theta = 0$ deg, (c) $d = 313$ mm and $\theta = 0$ deg, (d) $d = 300$ mm and $\theta = 1$ deg, (e) $d = 300$ mm and $\theta = -1$ deg, (f) $d = 306.5$ mm and $\theta = 1$ deg

grating, that is, $d = 306.5$ mm and $\theta = 1$ deg. Note that a combined translation and rotation of the transmission diffraction grating results in a change of both the magnitude and the direction of the reference grating vector **g**. In all cases, that is, in Figs. 9(d) to 9(f), several carrier fringes were added to the initial null-field moiré interference image.

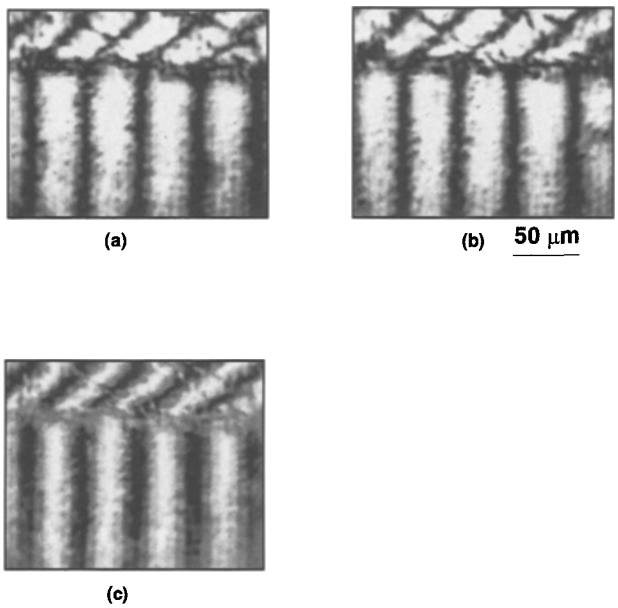

Fig. 10—Various steps in the digital processing of moiré interference fringe images: (a, b) moiré interference fringe image intensity distribution shifted by π, (c) resultant intensity obtained after subtraction of the images depicted in (a) and (b)

In general, the intensity of the incident beams used in the formation of the moiré interference fringe patterns is not uniform over the entire interference volume. Also, the efficiency of the specimen grating is not uniform and can vary with position. These factors along with aberration of the optical imaging system result in a slowly varying intensity of the moiré interference image and can lead to substantial background noise. To minimize these effects from the moiré interference fringe pattern, a relative phase of magnitude π is introduced between the two incident beams.[3,8] Figures 10(a) and 10(b) show two moiré interference images obtained by employing incident beams with a relative phase of ϕ_o and $\phi_o + \pi$, respectively. The subtracted image is shown in Fig. 10(c). The image subtraction process removes most of the background noise present in the images.

In most conventional moiré fringe analysis procedures, the moiré fringes are reduced to simple black-and-white patterns (two-level binarization). Using the resulting binary image, the fringe centerlines are located and stored as line segments to be used later to determine the fractional fringe number on a regularly spaced grid of points. This discrete moiré fringe analysis procedure has inherent shortcomings. First, the algorithm replaces any variation in phase in between the fringe centerlines by a constant phase gradient. Second, in the regions that do not lie in between the moiré fringes, that is, the region lying in between the image boundary and its neighboring moiré fringe, the phase information cannot be calculated. This problem becomes critical when the moiré fringe density in the image is sparse or the direction of the fringes in the moiré interference fringe pattern is nearly parallel to the direction in which the phase gradient is being calculated.

As mentioned previously, several methods including phase-stepping methods/algorithms have recently been developed to extract the phase information from the moiré interference images. In the present investigation, the displacement light-intensity moiré optical law put forward by Sciammarella[1] is revisited to obtain the displacement information from moiré fringe patterns. Figure 11(a) shows a typical **u** field moiré interference fringe pattern. Following Sciammarella,[1] the intensity $I(\mathbf{x})$ corresponding to the image shown in Fig. 11(a) can be expressed in terms of the first harmonic as

$$I(\mathbf{x}) = A(\mathbf{x}) + B(\mathbf{x})\cos(\psi(\mathbf{x})), \tag{24}$$

where the spatial function $A(\mathbf{x})$ represents the offset and $B(\mathbf{x})$ represents the amplitude of the intensity variation. Next, a normalized intensity distribution $\bar{I}(\mathbf{x})$ is sought such that

$$\bar{I}(\mathbf{x}) = \frac{I(\mathbf{x}) - A(\mathbf{x})}{B(\mathbf{x})} = \cos(\psi(\mathbf{x})). \tag{25}$$

Once the normalized intensity distribution $\bar{I}(\mathbf{x})$ is obtained, the phase distribution $\psi(\mathbf{x})$ can be readily unwrapped such that

$$\psi(\mathbf{x}) = \arccos\left(\bar{I}(\mathbf{x})\right). \tag{26}$$

To obtain the normalized intensity distribution $\bar{I}(\mathbf{x})$, the spatial functions $A(\mathbf{x})$ and $B(\mathbf{x})$ must be calculated from the moiré interference fringes. To obtain the functions $A(\mathbf{x})$ and $B(\mathbf{x})$, Sciammarella[1] had related them to the transmission function of the superimposed grids and the characteristics of the optical system forming the image. It was assumed that the moiré grid had ideal efficiency and that the optical system was free from aberrations and perfectly focused.

In the present investigation, digital image analysis is used to obtain the functions $A(\mathbf{x})$ and $B(\mathbf{x})$ from the actual moiré interference images acquired during the experiment. In this approach, first the lines representing the loci of all the local maximum intensity points of each moiré fringe and the lines representing the loci of all the local minimum intensity points of each fringe are digitally located. Next, two surfaces are calculated: surface $H(\mathbf{x})$, which envelopes the loci of all the local maximum intensity points of the moiré fringe pattern, and surface $L(\mathbf{x})$, which envelopes all the local minimum intensity points. These surfaces are shown for the moiré interference fringe pattern in Fig. 11(b). To obtain these surfaces, the biharmonic spline interpolation algorithm[16] was used. For N data points in two dimensions, the problem is reduced to finding the biharmonic function $w(\mathbf{x})$ that passes through the data points w_i located at $\mathbf{x}_i$, that is,

$$\nabla^4 w(\mathbf{x}) = \sum_{j=1}^{N} \alpha_j \delta\left(\mathbf{x} - \mathbf{x}_j\right) \tag{27}$$

and

$$w(\mathbf{x}_i) = w_i. \tag{28}$$

In eq (27), ∇^4 is the biharmonic operator, δ is the Kronecker delta, $\mathbf{x}$ is the position in the two-dimensional space and α_j is the weight corresponding to the point x_j. The general solution is given by

$$w(\mathbf{x}) = \sum_{j=1}^{N} \alpha_j \phi\left(\mathbf{x} - \mathbf{x}_j\right), \tag{29}$$

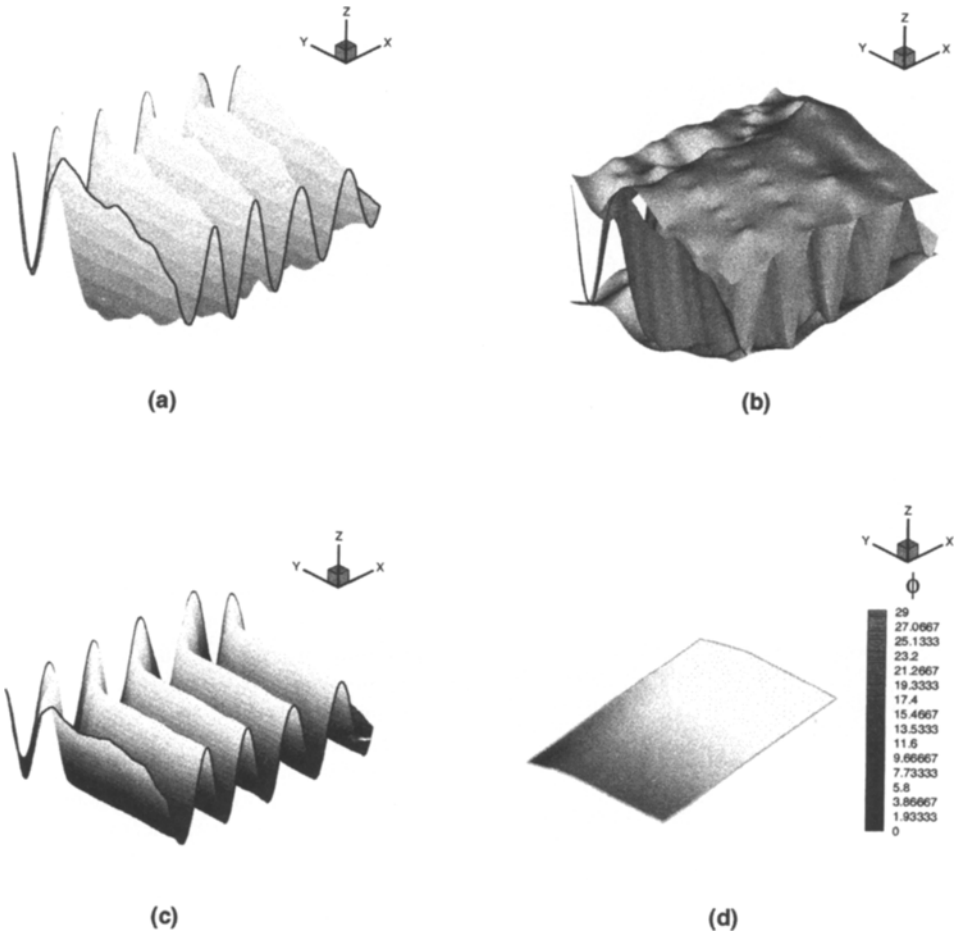

Fig. 11—Various steps in the moiré interference image analysis procedure: (a) intensity of the **u**-field moiré interference fringe pattern, (b) upper $[H(\mathbf{x})]$ and lower $[L(\mathbf{x})]$ surfaces that envelop the intensity profiles from above and below, (c) normalized intensity image obtained by employing eq (28) in text, (d) unwrapped phase obtained from the normalized intensity image in (c)

where the biharmonic Green's function $\phi = 2|\mathbf{x}|(\ln|\mathbf{x}| - 1)$. α_j are found by solving the linear system

$$w_i = \sum_{j=1}^{N} \alpha_j \phi\left(\mathbf{x}_i - \mathbf{x}_j\right). \tag{30}$$

Once the envelopes $H(\mathbf{x})$ and $L(\mathbf{x})$ are obtained, the functions $A(\mathbf{x})$ and $B(\mathbf{x})$ are obtained at each pixel location of the moiré interference fringe pattern by using

$$\begin{aligned} A(\mathbf{x}) &= \frac{1}{2}(H(\mathbf{x}) + L(\mathbf{x})) \\ B(\mathbf{x}) &= \frac{1}{2}(H(\mathbf{x}) - L(\mathbf{x})). \end{aligned} \tag{31}$$

Using (27) in (25), the intensity distribution of the entire image can be normalized between ± 1. The normalized intensity image corresponding to Fig. 11(a) is shown in Fig. 11(c).

Next, the phase is unwrapped by using eq (26) [shown in Fig. 11(d)]. The gradient of the phase at each pixel location is obtained by numerical differentiation. To obtain the gradient of the phase at a typical point $X(m, n)$, a user-defined $2N+1$ point interval is chosen in either direction. The N used in current analysis is 5, so the gage length corresponds to 10 pixels. Smaller intervals are used for points that do not have enough points on either side to form the $X(m-N : m+N, n)$ intervals, for example, the points near the image boundary. To calculate the phase gradient in the desired direction, a best-fit straight line is fitted through the $2N + 1$ points using the least squares principle. The slope of this line, also referred to as the regression coefficient, is the phase gradient.

By the use of this algorithm, any variations in phase in between the moiré interference fringes is accurately accounted for in the deformation analysis. Also, the algorithm allows us to accurately calculate the phase in the regions in between the image boundary and the neighboring fringes. Figures 12(a) to 12(c) represent the contours of the components of the deformation gradient tensor obtained using the phase gradient. As expected, the F11 and the F22 components are close to 1 over the entire region of interrogation. The upper half of Fig. 12(b) corresponds to the relatively soft solder layer and shows considerable deformation. Once the components of the deformation gradient tensor are obtained, eqs (10) to (20) can be used to calculate the local micro-mechanical quantities of interest, that is, the Almansi strain tensor, the principal stretches (and their directions) and the finite rotation tensor. Figure 13(a) shows the contour plot of the E12 component of the Almansi strain tensor, $\mathbf{E}^{\mathbf{A}}$. Note the inhomogeneity in the local deformation. Maximum plastic strains of 4 percent to 5 percent were obtained. Figure 13(b) shows the contour plot of the local rotation of the material during the deformation.

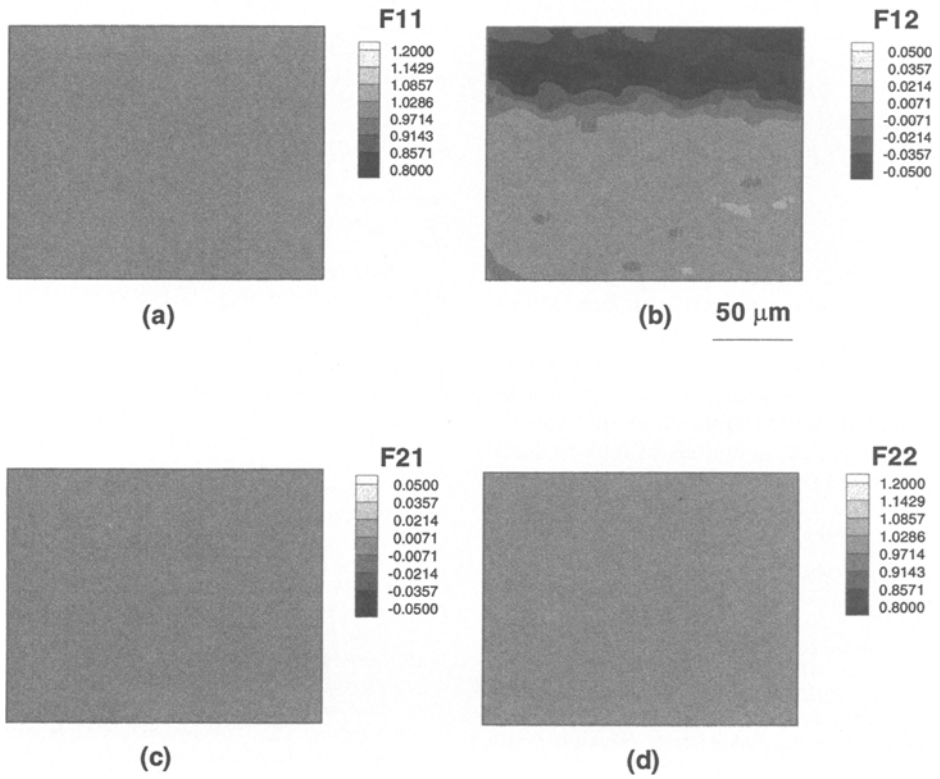

Fig. 12—Contour plots showing the components of the deformation gradient tensor: (a) F11 component, (b) F12 component, (c) F21 component, (d) F22 component

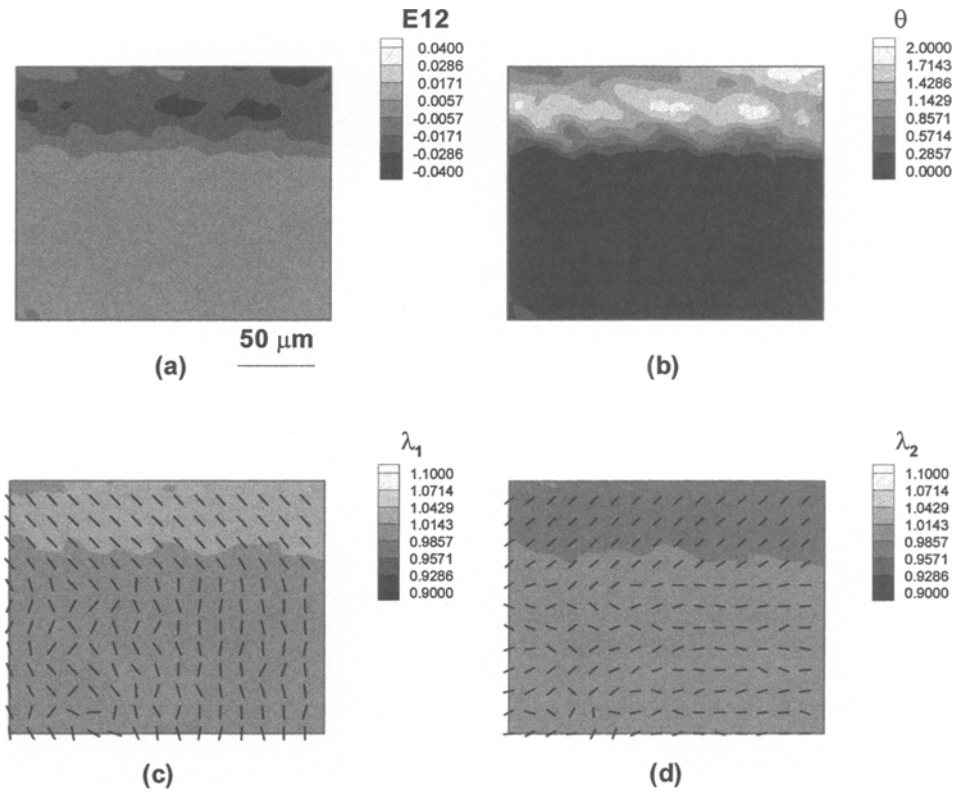

Fig. 13—Contour plots showing the components of the Almansi strain tensor: (a) E12 component, (b) contour plot showing the magnitude of the local material rotation in degrees, (c) contour plot showing the magnitude of the first principal stretch (the superposed vector plot shows the direction of the first principal stretch), (d) contour plot showing the magnitude of the second principal stretch (the superposed vector plot shows the direction of the second principal stretch)

Maximum local rotations of approximately 2 degrees can be observed. Figures 13(c) and 13(d) show the magnitude as well as the principal directions of the first principal and the second principal stretches. The gray-scale levels represent the magnitude of the principal stretch, while the dashed lines superimposed on the contour plots show the direction of the principal stretch.

Conclusions

A new version of a moiré microscope is presented that embodies the theory of optical moiré interferometry. Moreover, an interactive image-processing program is developed to acquire the moiré interference images and carry out deformation analysis. The deformation analysis is consistent with the continuum principles of finite deformation, and can be used to obtain micro-mechanical quantities of interest such as local strains, stretches and rotations.

References

1. *Sciammarella, C.A., "Basic Optical Law in the Interpretation of Moiré Patterns Applied to the Analysis of Strains—Part I,"* EXPERIMENTAL MECHANICS, **5**, *154–160 (1965).*

2. *Rayleigh, L., "On the Manufacture and Theory of Diffraction Gratings," The Philosophical Magazine,* **47** *(81), 193 (1874).*

3. *Post, D., Han, B., and Ifju, P., High Sensitivity Moiré: Experimental Analysis for Mechanics and Materials, Springer-Verlag, New York (1994).*

4. *Theocaris, P.S., Moiré Fringes in Strain Analysis, Pergamon Press, New York (1969).*

5. *Durelli, A.J. and Parks, V.J., Moiré Analysis of Strain, Prentice Hall, Englewood Cliffs, NJ (1970).*

6. *Parks, V.J., "Geometric Moiré: Chapter 6," Handbook on Experimental Mechanics, 2d ed., VCH, New York (1993).*

7. *Chiang, F.-P., "Moiré Methods of Strain Analysis: Chapter 7," Manual on Experimental Mechanics, 5th ed., Society for Experimental Mechanics, Bethel, CT (1989).*

8. *Shield, T.W. and Kim, K.-S., "Diffraction Theory of Optical Interference Moiré and a Device for Production of Variable Virtual Reference Grating: A Moiré Microscope,"* EXPERIMENTAL MECHANICS, **31**, *126–134 (1991).*

9. *Han, B. and Post, D., "Immersion Interferometer for Microscopic Moiré Interferometry,"* EXPERIMENTAL MECHANICS, **32**, *38–41 (1992).*

10. *Zou, D., Zhu, J., Dai, F., Liu, S., and Guo, Y.-F., "Global/Local Thermal Deformation Study of Power Plastic Package by a Multipurpose Macro/Micro Moiré Interferometer," Abstract Proceedings of the 1997 SEM Spring Conference on Experimental Mechanics, Bellevue, Washington.*

11. *Dally, J.W. and Read, D.T., "Electron Beam Moiré,"* EXPERIMENTAL MECHANICS, **33**, *270–277 (1993).*

12. *Sciammarella, C.A. and Durelli, A.J., "Moiré Fringes as a Means of Analyzing Strains," Trans. Am. Soc. Civil Engineers,* **127** *(Part 1), 582–603 (1962).*

13. *Perry, K.E. and McKelvie, J., "A Comparison of Phase Shifting and Fourier Methods in the Analysis of Discontinuous Fringe Patterns," Opt. Lasers Eng.,* **19**, *269–285 (1993).*

14. *Han, B., "Interferometric Methods with Enhanced Sensitivity by Optical/Digital Fringe Multiplication," Appl. Opt.,* **32**, *4713–4718 (1993).*

15. *Gurtin, M.E., An Introduction to Continuum Mechanics, Academic Press, New York (1981).*

16. *Sandwell, D.T., "Biharmonic Spline Interpolation of GEOS-3 and Seasat Altimeter Data," Geophys. Res. Lett.,* **2**, *139–142 (1987).*